The Astrophysical Journal, 794:3 (15pp), 2014 October 10 doi:10.1088/0004-637X/794/1/3

HOT JUPITERS AND COOL STARS

Eva Villaver[1], Mario Livio[2], Alexander J. Mustill[1,3], and Lionel Siess[4]
[1] Department of Theoretical Physics, Universidad Autónoma de Madrid, Módulo 8, 28049 Madrid, Spain; eva.villaver@uam.es
[2] Space Telescope Science Institute, 3700 San Martin Drive, Baltimore, MD 21218, USA
[3] Department of Astronomy and Theoretical Physics, Lund University, Box 43, SE-221 00 Lund, Sweden
[4] Institut d'Astronomie et d'Astrophysique, Université Libre de Bruxelles, B-1050 Bruxelles, Belgium
Received 2014 April 9; accepted 2014 July 25; published 2014 September 17

ABSTRACT

Close-in planets are in jeopardy, as their host stars evolve off the main sequence (MS) to the subgiant and red giant phases. In this paper, we explore the influences of the stellar mass (in the range 1.5–2 $M_{\odot}$), mass-loss prescription, planet mass (from Neptune up to 10 Jupiter masses), and eccentricity on the orbital evolution of planets as their parent stars evolve to become subgiants and red giants. We find that planet engulfment along the red giant branch is not very sensitive to the stellar mass or mass-loss rates adopted in the calculations, but quite sensitive to the planetary mass. The range of initial separations for planet engulfment increases with decreasing mass-loss rates or stellar masses and increasing planetary masses. Regarding the planet's orbital eccentricity, we find that as the star evolves into the red giant phase, stellar tides start to dominate over planetary tides. As a consequence, a transient population of moderately eccentric close-in Jovian planets is created that otherwise would have been expected to be absent from MS stars. We find that very eccentric and distant planets do not experience much eccentricity decay, and that planet engulfment is primarily determined by the pericenter distance and the maximum stellar radius.

Key words: planetary systems – stars: evolution – stars: fundamental parameters – stars: general

Online-only material: color figures

1. INTRODUCTION

Planets orbiting evolved stars offer opportunities to explore a wide range of physical processes that are not applicable to main-sequence (MS) hosts. These processes include orbital evolution under the influence of tides and mass loss, planetary ejection or evaporation, instabilities, and the evolution of binary systems (e.g., Villaver & Livio 2007, 2009; Duncan & Lissauer 1998; Debes & Sigurdsson 2002; Kunitomo et al. 2011; Bear & Soker 2011; Mustill & Villaver 2012; Nordhaus et al. 2010; Nordhaus & Spiegel 2013; Moeckel & Veras 2012; Kratter & Perets 2012; Veras et al. 2011, 2013).

Observations show that there is a deficiency of close-in planets around evolved stars (Johnson et al. 2007; Lovis & Mayor 2007; Sato et al. 2007) compared to their MS counterparts, even though the two samples have been observed using the same radial velocity technique (e.g., Johnson et al. 2007; Sato et al. 2008; Wright et al. 2009; Niedzielski et al. 2009). The masses of these evolved stars derived from stellar model fitting are typically higher than those of MS planet hosts. At the same time, evolved stars that are hosting planets do not seem to show differences in their Galactic velocity distribution from F5–G5 MS stars (Schlaufman & Winn 2013; Maldonado et al. 2013), suggesting that the masses of the evolved stars are similar to MS planet hosts.

Two different mechanisms (not necessarily mutually exclusive) have been proposed to explain the distribution of planetary orbits around evolved stars. One is based on the dispersal timescale of protoplanetary disks and is directly related to the stellar mass (e.g., Currie 2009), and the other relies on tidal interaction and orbital decay (e.g., Villaver & Livio 2009). The former mechanism requires the masses of the evolved stars to be higher than those of the MS hosts. Whether or not this condition is consistent with observations has recently been a topic of some debate (Lloyd 2013; Schlaufman & Winn 2013; Johnson et al. 2013).

The fact remains, however, that both stellar evolution and tidal interaction still involve considerable uncertainties. For instance, the prescription used for mass loss affects the orbital evolution both directly as winds carry away angular momentum, and through its effects on the stellar radius (and thereby on tidal interaction). The ratio of planet mass to stellar mass also strongly affects tides. Previous studies of the orbital evolution of planetary systems around red giant branch (RGB) stars did not investigate either the effects of the adopted mass-loss prescription or the planet's eccentricity evolution (e.g., Villaver & Livio 2009; Kunitomo et al. 2011), or focus on large orbital distances (Veras et al. 2011) or on the outcome of the orbital evolution in a later stage, the asymptotic giant branch phase, and its relevance for the detection of systems during the white dwarf phase (Nordhaus et al. 2010; Nordhaus & Spiegel 2013; Mustill & Villaver 2012). Although a range of stellar masses has been considered by Kunitomo et al. (2011), their tidal evolution calculation was greatly simplified because of the unavailability of the internal stellar structure needed for the calculation in their models.

In this work, we present detailed, self-consistent, stellar models coupled with orbital evolution. Our computational grid encompasses the evolution from the MS and up to the onset of helium burning in the stellar core. We have selected a range of stellar masses from 1.5 $M_{\odot}$ to 2 $M_{\odot}$, in steps of 0.1 $M_{\odot}$, and for each stellar mass we have computed the evolution of the star with three different prescriptions for the mass loss. For each star, we have calculated the orbital evolution with planetary masses corresponding that of Neptune, and to 1, 2, 5, and 10 Jupiter masses. We have also considered the planet's eccentricity evolution. Our goal is to characterize and quantify the effects of mass loss, stellar mass (in an interesting range), planetary

mass, and eccentricity on planet survival during the RGB phase.

2. THE CALCULATIONS

We follow the same procedure as in Villaver & Livio (2009, hereafter VL09) and Mustill & Villaver (2012) to determine the planet orbital and eccentricity evolution as the star evolves off the MS and up the RGB. We take into account the changes in the mass of the star, the gravitational and frictional drag, and the tidal force. We have not evaluated in this paper either the accretion onto, or the ablation of matter from, the surface of the planet. Based on the estimates provided by the prescription given in VL09, we find that the effect of mass loss from the star dominates over those processes, even when small RGB mass-loss rates are considered.

We use three different prescriptions for the mass loss in this paper, two that follow a Reimers' law valid for red giants (Reimers 1975) and use values of η_R (the Reimers parameter) of 0.2 and 0.5 in the formula

$$\dot{M}_{\rm R} = 4\times10^{-13}\,\eta_R\frac{L_\star R_\star}{M_\star}\quad [M_\odot\,{\rm yr}^{-1}], \tag{1}$$

and a third one based on the new semiempirical relation provided by Schröder & Cuntz (2005):

$$\dot{M}_{\rm Sc} = \eta\frac{L_\star R_\star}{M_\star}\left(\frac{T_{\rm eff}}{4000\,{\rm K}}\right)^{3.5}\left(1+\frac{g_\odot}{4300 g_\star}\right)\quad [M_\odot\,{\rm yr}^{-1}], \tag{2}$$

where $L_\star$, $R_\star$, $g_\star$, and $M_\star$ are the stellar luminosity, radius, surface gravity, and mass, respectively (in solar units), and the factor $\eta = 8\times10^{-14}$ has been obtained by fitting the theoretical relation to observations of globular clusters with different metallicities; $g_\odot$ is the Sun's surface gravity. Thus, the rate of change of the stellar mass is simply given by $\dot{M}_\star = -\dot{M}_{\rm R}$, or $\dot{M}_\star = -\dot{M}_{\rm Sc}$. The stellar evolution calculations have been self-consistently carried out using these three mass-loss prescriptions (see Section 2.1 for details).

We consider that a planet of mass M_p and radius R_p is orbiting with a velocity v a star of mass $M_\star$. Conservation of angular momentum gives an equation for the rate of change in the semimajor axis of the planet, assuming that the timescale for mass loss is much greater than the orbital timescale (see, e.g., Alexander et al. 1976; Livio & Soker 1984; Villaver & Livio 2009; Mustill & Villaver 2012),

$$\left(\frac{\dot{a}}{a}\right) = -\frac{\dot{M}_\star}{M_\star+M_p} - \frac{2}{M_p v}[F_f+F_g] - \left(\frac{\dot{a}}{a}\right)_t, \tag{3}$$

where $(\dot{a}/a)_t$ is the rate of orbital decay due to the tidal interaction and F_f and F_g are, respectively, the frictional and gravitational drag forces that have been computed with the prescription given in VL09. The frictional force is expressed in the form (e.g., Rosenhead 1963)

$$F_f = \frac{1}{2}C_d\rho v^2\pi R_p^2, \tag{4}$$

where $C_d \simeq 0.9$ is the dimensionless drag coefficient for a sphere, and the gravitational drag force, F_g, has a funtional form given by (e.g., Ostriker 1999, and references therein)

$$F_g = 4\pi\frac{(GM_p)^2}{c_s^2}\rho I, \tag{5}$$

where for I we used the value $I \simeq 0.5$, which is appropriate for the range of Mach numbers for this problem.

We consider tides acting on both the planet and the star. For the planetary tides, we use the formalism of Dobbs-Dixon et al. (2004) with a fixed tidal dissipation efficiency parameter $Q'_{\rm pl}$, while for the stellar tides, we adopt the formalism of Zahn (1977), in which tidal energy is dissipated by turbulent motions in the star's convective envelope. In fact, in giant stars, which have massive convective envelopes, the most efficient mechanism to produce tidal friction is turbulent viscosity (e.g., Zahn 1966, 1977, 1989). For the angular momentum loss associated with the tidal term $(\dot{a}/a)_t$, the dissipation timescale is determined by the effective eddy viscosity, with eddy velocities and length scales given approximately by the standard mixing length theory if convection transports most of the energy flux (Zahn 1989; Verbunt & Phinney 1995; Rasio et al. 1996). The stellar tidal term is given by

$$\left(\frac{\dot{a}}{a}\right)_t = \frac{1}{9\tau_d}\frac{M_{\rm env}}{M_\star}q(1+q)\left(\frac{R_\star}{a}\right)^8 \times\left[2f_2+e^2\left(\frac{7}{8}f_1-10f_2+\frac{441}{8}f_3\right)\right], \tag{6}$$

and the planet eccentricity decays as

$$\frac{\dot{e}}{e} = -\frac{1}{36\tau_d}\frac{M_{\rm env}}{M_\star}q(1+q)\left(\frac{R_\star}{a}\right)^8\times\left[\frac{5}{4}f_1-2f_2+\frac{147}{4}f_3\right], \tag{7}$$

with $M_{\rm env}$ and $R_{\rm env}$ being the mass and radial extent of the convective envelope, respectively, $q = M_p/M_\star$, and τ_d is the eddy turnover timescale in the stellar envelope,

$$\tau_d = \left[\frac{M_{\rm env}\,(R_\star-R_{\rm env})^2}{3L_\star}\right]^{1/3}. \tag{8}$$

The frequency components f_i are given by

$$f_i = f'\,\min\left[1,\left(\frac{2\pi}{in c_{\rm F}\tau_d}\right)^\gamma\right], \tag{9}$$

where in, with n the mean motion, are the individual frequency components. As in VL09 and Mustill & Villaver (2012), we have used $c_{\rm F} = 1$, $f' = 9/2$ and a value of $\gamma = 2$, which is consistent with the results obtained from numerical calculations (e.g., Zahn 1977; Goldreich & Nicholson 1977; Penev et al. 2007).

In this study, we have made the particular choice of using turbulent convection for the dissipation of the equilibrium tide, so under our assumption, if the star does not have a convective envelope, there is no tide. For stars with radiative envelopes, the use of the Q formalism circumvents this problem by parameterizing the strength of the tidal forces into a variable $Q'_\star$. When the $Q'_\star$ parameter is calibrated using MS stars, it has values in the 10^5–10^{10} range (e.g., Jackson et al. 2008a, 2009; Penev & Sasselov 2011). However, for giant stars, a much smaller $Q'_\star \approx 10^2$–10^3 is found by Nordhaus et al. (2010) to be equivalent to the Zahn (1977) formalism. Note that since giant stars have deep convective zones, the most appropriate mechanism to describe the equilibrium tide is the one adopted here (e.g., Ogilvie 2014). Thus, it is inappropriate to apply the Q formalism using the MS calibration for our stars and will anyhow result in much weaker tides than assumed. We have

neglected other tidal mechanisms such as dynamical tides (e.g., Witte & Savonije 2002), which, although they may be important for massive stars during the MS, are mostly irrelevant for the computations for convective stars presented here.

Only during the MS phase might we have a non-convective star. Thus, for stars without a convection zone and in order to avoid numerical round-off errors, we set the convective timescale to an arbitrarily large value (10^9 years). Note that on the MS we are only studying the eccentricity evolution for which only the planetary tides are important.

For eccentric orbits, we have also implemented a planetary tide using the standard Q model (e.g., Matsumura et al. 2010). The planet's semimajor axis, eccentricity, and spin rate then evolve according to

$$\frac{\dot{e}}{e} = -\frac{81n}{2Q'_{\rm p}}\frac{1}{q}\left(\frac{R_{\rm p}}{a}\right)^5 \times\left[g_3(1-e^2)^{-13/2} - \frac{11g_4(1-e^2)^{-5}\Omega_{\rm p}}{18n}\right] \quad (10)$$

$$\frac{\dot{a}}{a} = \frac{2e\dot{e}}{1-e^2} - \frac{9}{Q'_{\rm p}}\frac{1}{q}\left(\frac{R_{\rm p}}{a}\right)^5 \times\left[g_2(1-e^2)^{-13/2}n - g_5(1-e^2)^{-5}\Omega_{\rm p}\right] \quad (11)$$

$$\dot{\Omega}_{\rm p} = \frac{9n^2}{2\alpha_{\rm p}Q'_{\rm p}}\frac{1}{q}\left(\frac{R_{\rm p}}{a}\right)^3 \times\left[g_2(1-e^2)^{-6} - g_5(1-e^2)^{-4.5}\frac{\Omega_{\rm p}}{n}\right], \quad (12)$$

where $R_{\rm p}$ is the planet's radius. The eccentricity functions g_i are given by

$$g_2 = 1 + \frac{15}{2}e^2 + \frac{45}{8}e^4 + \frac{5}{16}e^6 \quad (13)$$

$$g_3 = 1 + \frac{15}{4}e^2 + \frac{15}{8}e^4 + \frac{5}{64}e^6 \quad (14)$$

$$g_4 = 1 + \frac{3}{2}e^2 + \frac{1}{8}e^4 \quad (15)$$

$$g_5 = 1 + 3e^2 + \frac{3}{8}e^4. \quad (16)$$

We note that while the planet tidal equations are valid for arbitrary planet eccentricities, the stellar tidal equations are based on the lowest-order expansion of the equations and are not strictly valid when the planetary eccentricity is high (note that in Zahn (1989) the $\dot{a}$ equation is valid for any eccentricity, but he uses the weak approximation). The reason for this lies in the stellar tidal model; the different Fourier components have different frequency dependencies, and as the eccentricity rises, higher-frequency Fourier components come into play. Nevertheless, for this exploratory study, we used the truncated equations even for highly eccentric planets, deferring a full expansion of the tidal forces to future work. It is important to keep in mind as well that, as discussed in Mustill & Villaver (2012), the parameters in the tidal equations are poorly known, and consequently the tidal forces may be stronger or weaker than assumed here.

The main uncertainty in the tidal model used comes from the need to reduce the effective viscosity when the tidal period is short compared to the typical convective timescale (e.g., Ogilvie 2014). This is taken into account by variations in the power index γ in Equation (9). As γ increases, the tidal dissipation becomes less efficient, but only when the planet's orbital period is shorter than the eddy turnover timescale in the stellar envelope. We have chosen $\gamma = 2$ in Equation (9), consistent with the results of Ogilvie & Lesur (2012); earlier results of Penev et al. (2007) suggested $\gamma = 1$.

The tidal model is only sensitive to the assumed value of γ for small orbital distances when the stellar radius is small (e.g., Kunitomo et al. 2011). Thus, variations in the power index will not lead to any significant changes in the final outcome of our planets since we are dealing with stars that reach a large radius at the tip of the RGB. If the planet has such a short orbital period necessary to be sensitive to the adopted γ, then it would be engulfed very early by the expansion of the star.

Measurements of the spin rates of giants provide average values of $v \sin i \leqslant 2$ km s^{-1}(e.g., de Medeiros et al. 1996; Massarotti et al. 2008), with rapid rotators found only in a few percent (1%–2%) of giant stars (Carlberg et al. 2011). These observations justify our assumption of using non-rotating stars for the calculation of tidal forces. Planet spin rates were allowed with values between 10 and 1000 rad/yr.

A proper calculation of the stellar tides requires knowledge of the stellar structure (i.e., $M_{\rm env}$ and $R_{\rm env}$). Note that some calculations in the literature do not have this information, and as result they rely on simplifications such as the assumption that $M_{\rm env} = M_\star$ and $R_{\rm env} = 0$ for the evaluation of the effects of tidal dissipation on the planet's orbital evolution.

2.1. The Stellar Models

The stellar evolution models were calculated with the STAREVOL code (Siess 2006). We have computed a small grid of non-rotating models with initial masses in the range of 1.5 and 2 $M_\odot$, in mass steps of 0.1 $M_\odot$. Based on the observations by Maldonado et al. (2013), we have chosen a stellar metallicity that fullfils two requirements: (1) it is consistent with the observed metallicity of planet-hosting giant stars with stellar masses $M_\star > 1.5\,M_\odot$, and (2) it agrees with the observed metallicities of subgiant stars with planets detected. The initial metallicity is thus set to [Fe/H] = 0.19 with a composition scaled solar according to Grevesse et al. (1996). We do not consider any "extra-mixing processes" such as overshooting or thermohaline mixing and use the Schwarzschild criterion to define the convective boundaries. We adopt $\alpha_{\rm MLT} = 1.75$ for the mixing length parameter, which was determined from solar fitting models. As described above, we considered three representative mass-loss rate prescriptions (see Equations (1) and (2)).

The extent of the RGB on the H-R diagram is very sensitive to the stellar mass for values around the transition mass that marks the border between degenerate and non-degenerate cores. We use here RGB models with masses lower than 2.0 $M_\odot$ because they develop electron degenerate He cores after the end of central H-burning for solar metallicity. These stars have an extended and luminous RGB phase prior to Helium ignition and therefore represent the most interesting arena for the problem analyzed in this paper. The maximum stellar luminosity at the tip of the RGB is reached for stars with degenerate cores and it translates into a maximum stellar radius reached during the RGB.

Table 1
Stellar Model Properties

$M_{\rm ini}$ [$M_\odot$]	Wind	$M_{\rm 1DUP}$ [$M_\odot$]	$M_{\rm tip}$ [$M_\odot$]	$R_{\rm tip}$ [$R_\odot$]	$L_{\rm tip}$ [$L_\odot$]	$M_{\rm tip}^{\rm core}$ [$M_\odot$]	$\dot{M}_{\rm tip}$ [$M_\odot$/yr]	$t_{\rm RGB}$ [Myr]	a_c, $M_p = M_J$ [AU]
1.5	$\eta_R = 0.2$	1.497	1.410	216.2	3015.4	0.489	3.469×10^{-8}	203.9	2.43
1.5	$\eta_R = 0.5$	1.494	1.304	196.4	2560.4	0.472	7.251×10^{-8}	203.6	2.11
1.5	$\eta_R = 0.5$+OS	1.494	1.272	221.9	2913.2	0.485	9.465×10^{-8}	197.5	2.10
1.5	Sc	1.490	1.369	190.3	2547.7	0.471	6.834×10^{-8}	206.3	2.14
1.6	$\eta_R = 0.2$	1.597	1.516	209.2	3027.7	0.490	3.152×10^{-8}	185.1	2.38
1.6	$\eta_R = 0.5$	1.594	1.393	209.4	2871.6	0.483	8.105×10^{-8}	186.6	2.20
1.6	Sc	1.589	1.448	209.4	2960.1	0.486	8.924×10^{-8}	190.1	2.04
1.7	$\eta_R = 0.2$	1.697	1.620	204.8	3072.7	0.491	2.946×10^{-8}	190.2	2.34
1.7	$\eta_R = 0.5$	1.694	1.519	191.2	2705.1	0.477	6.458×10^{-8}	190.3	2.09
1.7	$\eta_R = 0.5$+OS	1.694	1.509	201.8	2888.1	0.484	7.300×10^{-8}	154.2	2.07
1.7	Sc	1.688	1.590	176.8	2542.8	0.470	4.904×10^{-8}	176.7	2.03
1.8	$\eta_R = 0.2$	1.797	1.724	202.2	3128.0	0.493	2.791×10^{-8}	161.5	2.29
1.8	$\eta_R = 0.5$	1.794	1.638	177.1	2569.4	0.472	5.300×10^{-8}	162.5	1.99
1.8	Sc	1.787	1.686	181.9	2716.6	0.477	5.108×10^{-8}	183.9	2.09
1.9	$\eta_R = 0.2$	1.898	1.827	198.2	3155.4	0.493	2.613×10^{-8}	149.9	2.25
1.9	$\eta_R = 0.5$	1.894	1.727	190.1	2898.6	0.484	6.082×10^{-8}	149.3	2.09
1.9	$\eta_R = 0.5$+OS	1.894	1.732	191.0	2934.7	0.486	6.170×10^{-8}	86.9	2.09
1.9	Sc	1.885	1.786	184.2	2847.2	0.481	5.091×10^{-8}	146.1	2.09
2.0	$\eta_R = 0.2$	1.997	1.930	193.9	3166.5	0.494	2.434×10^{-8}	148.7	2.21
2.0	$\eta_R = 0.5$	1.995	1.821	198.6	3155.7	0.494	6.560×10^{-8}	145.9	2.15
2.0	Sc	1.984	1.874	196.0	3173.7	0.494	6.032×10^{-8}	160.2	2.19

Higher-mass stars can ignite helium quietly, terminating the ascent up the RGB before electron degeneracy becomes appreciable in the core, and they reach smaller radii than stars with degenerate cores. Note, however, that the precise value of the transition mass between low- and intermediate-mass stars depends on the initial chemical composition (e.g., Sweigart et al. 1989, 1990). Decreasing the initial Helium abundance or increasing the heavy element abundances leads to higher transition stellar masses. Thus, for stars born in higher metallicity environments, we have larger initial masses marking the transition between degenerate and non-degenerate He cores.

We summarize in Table 1 some of the properties of our stellar models. Column (1) gives the initial mass; Column (2) the mass-loss prescription used, where Sc refers to the Schröder & Cuntz (2005) model and $\eta_R = 0.5 + OS$ is a model with overshooting; Column (3) gives the stellar mass at the time of the deepest extent of the convective envelope during the first dredge-up (1DUP); Columns (4), (5), and (6) give the stellar mass, radius, and luminosity at the tip of the RGB, respectively; Column (7) provides the mass of the hydrogen depleted core; Column (8) the mass-loss rate at the tip of the RGB; and Column (9) gives the duration of the RGB phase between the time of the 1DUP and the RGB tip. Finally, Column (10) gives the minimum initial orbital distance to avoid engulfment at the tip of the RGB calculated for a planet with the mass of Jupiter.

3. RESULTS

As hydrogen becomes exhausted at the center of the star, core contraction accelerates and the star leaves the MS on the H-R diagram. The major energy production source shifts to a thick shell outside the core where shell ignition drives envelope expansion and causes the stellar radius to increase (e.g., Iben 1967). Shortly after the star reaches the base of the RGB, convection expands inward from the surface and the first dredge-up takes place.

The planet's orbital evolution was computed by solving the system of Equations (3)–(16) coupled with the stellar structure evolution. We did so for each of the six stellar masses and three mass-loss prescriptions considered (a total of 18 stellar models) and we used five planetary masses. For each of these 90 models, we then calculated the orbital evolution by varying the initial orbital separation between 0.1 and 3.5 AU using steps of 0.01 AU. Every integration timestep included an update of the stellar structure (fundamental for an accurate calculation of the stellar tide) and of the variable mass-loss rates. We also introduced a constraint in the orbital integration timestep so that it was never larger than the timestep at which a significant change in the stellar structure took place.

We first consider circular orbits ($e = 0$) in Equations (6) to (16) to investigate the effects of changing the stellar models. For the systems considered in this paper, tidal dissipation in the star dominates (see, e.g., Matsumura et al. 2010), and thus we justify circular orbits (for now) on the basis of the fact that both the eccentricity and the semimajor axis damp on similar timescales (Mustill & Villaver 2012). Note as well that the initial value of the eccentricity has little effect on the orbital decay rate (e.g., Jackson et al. 2008a, 2008b).

We first focus on estimating variations induced by varying parameters such as mass loss, stellar mass, and planet mass, and we defer the discussion of eccentric orbits to Section 3.4.

The combined effects of tidally induced orbital decay and mass-loss-induced orbital expansion modifies the orbit of the planets in a simple way. If the initial planet separation is within a certain range of distances from the star, the planet will experience an orbital decay caused by the tidal interaction. This ends with the planet plunging into the stellar envelope. If, on the other hand, the initial orbit is beyond a certain radius, the planet avoids engulfment.

Figure 1 shows a Jupiter-mass planet's orbits during $\approx$0.06 Gyr along the RGB phase for a range of initial orbital distances and a particular stellar model (1.5 $M_\odot$ with the Schröder & Cuntz 2005 mass-loss prescription). A few features in Figure 1 are worth noting. First, marked with a solid black line is the initial orbital distance beyond which the planet avoids falling into the stellar envelope during the RGB phase.

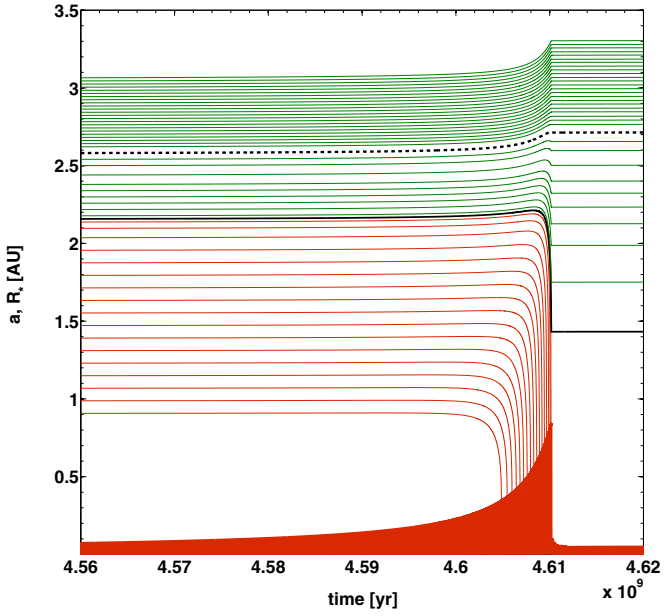

Figure 1. Filled red area represents 0.06 Gyr in the evolution of the stellar radius as the star goes to the tip of the RGB. The star has a mass of 1.5 $M_{\odot}$ and is evolving under the Schröder & Cuntz (2005) mass-loss prescription. The evolution of a set of orbits of a planet with 1 Jupiter mass is shown as well, with the red lines representing a set of initial separations for which the planet ends up inside the stellar envelope. The green lines represent the initial separations for which the planet avoids engulfment. The solid black line is the minimum initial orbit for which the planet avoids being engulfed and the dashed black line marks the initial orbit beyond which the planet is not affected by the tidal forces.

(A color version of this figure is available in the online journal.)

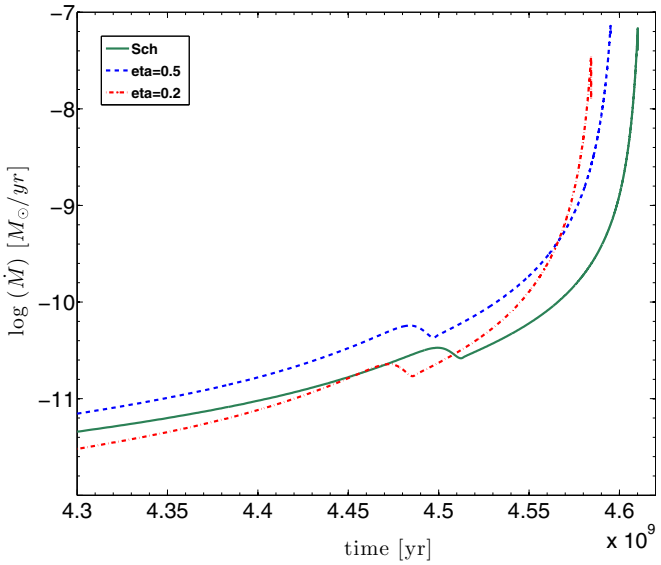

Figure 2. Mass-loss rates for 1.5 $M_{\odot}$ stars during the last years of the RGB evolution under $\eta_R = 0.2$ (red dot–dashed line), $\eta_R = 0.5$ (blue dashed line), and Schröder & Cuntz (2005; green solid line).

(A color version of this figure is available in the online journal.)

Every initial separation below the solid black line terminates with the planet being engulfed.

What happens to those planets that enter the envelope largely depends on the ratio of the planet's mass to the envelope mass. Many will end up merging with the stellar core, given the fast decay of the orbit induced by the strong drag forces (Nordhaus & Blackman 2006; Siess & Livio 1999a, 1999b). Rough estimates of planet survival inside stellar envelopes provide minimum masses of the order of 10–15 Jovian masses (again, depending also on the envelope's mass; Villaver & Livio 2007; Nordhaus et al. 2010). An analysis of the possible progenitors of the planets found orbiting the horizontal branch star KIC 05807616 (Charpinet et al. 2011) also concludes that the surviving planets likely had a mass of a few Jupiter masses (Passy et al. 2012). Note that for survival to occur, a planet must be able to supply enough of its orbital energy to the stellar envelope to unbind the latter before the planet spirals into the disruption region or the stellar core. Unfortunately, the efficiency of the process of unbinding (commonly parameterized with $\alpha_{\rm CE}$, e.g., Livio & Soker 1988) is rather uncertain. Given that the largest planet mass we are considering is 10 M_J, our working hypothesis in this paper is that whenever the planet gets inside the stellar envelope, it will be destroyed. We defer further discussion of planetary systems entering stellar envelopes for a forthcoming study.

The second important feature of the planet's orbital evolution that is important to mention is the range of initial orbital distances that experience tidal decay but that still manage to avoid entering the surface of the star. This range of orbits lies in Figure 1 close to the solid line. The dot–dashed black line shows a typical example of an orbit dominated by mass loss. The orbital decay can be substantial for initial orbits close to the critical limit (marked by the solid black line), with the planet ending up in a significantly tighter orbit than the initial one. Planets that start at orbital distances slightly larger than that marked by the solid line still experience the consequences of tidal forces, but once helium burning is ignited in the core, the star contracts and the interaction stops. Planets in this initial range do not reach the stellar envelope, but end up at smaller separations.

Beyond the dot–dashed line in Figure 1, the orbits increase due to mass loss from the system.

3.1. The Effects of RGB Mass Loss

Equation (3) clearly suggests that the critical orbital distance for engulfment, and the distance beyond which the separation is expected to increase, are sensitively dependent on the mass-loss prescription adopted in the calculations (for an analytical treatment of the problem, see Adams & Bloch 2013). The purpose of our self-consistent calculation, with models under different mass-loss prescriptions, is to quantify the influence of this relatively poorly constrained parameter on planet survival during the RGB evolution.

Along the RGB, the models under different mass-loss prescriptions show significant differences associated entirely with the way these stars are losing mass (see Table 1). The mass-loss rate along the RGB is relatively smooth (see Equations (1) and (2)) and never reaches high values (see Figure 2). The largest and smallest mass-loss rates are attained for the $\eta_R = 0.5$, and $\eta_R = 0.2$ prescriptions, respectively, with the Schröder & Cuntz (2005) model having mass-loss rates between these two values. In Figure 2, we have plotted the evolution of the mass loss under the three prescriptions used for the 1.5 $M_{\odot}$ model. In Figure 3, we show the stellar mass reached at the tip of the RGB versus the stellar MS mass.

We tried to capture the main differences in the planet survival limit among the models in Figure 4, where we show for the 1.5 $M_{\odot}$ star the different evolution of the stellar radius for the three mass-loss prescriptions considered (in red, blue, and

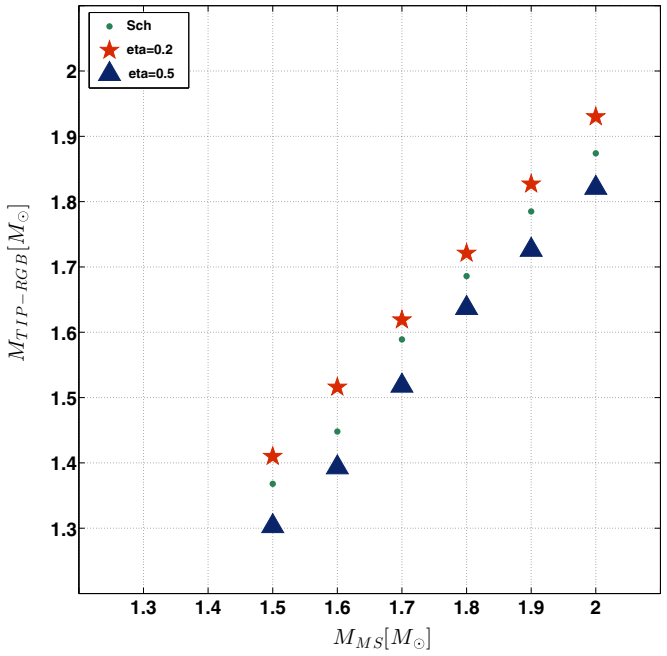

Figure 3. Mass of the star at the tip of the RGB in solar units vs. the MS mass of the star. The different symbols correspond to the three prescriptions used and are indicated in the legend (red stars ($\eta_R = 0.2$), blue triangles ($\eta_R = 0.5$), and green asterisks (Schröder & Cuntz 2005).

(A color version of this figure is available in the online journal.)

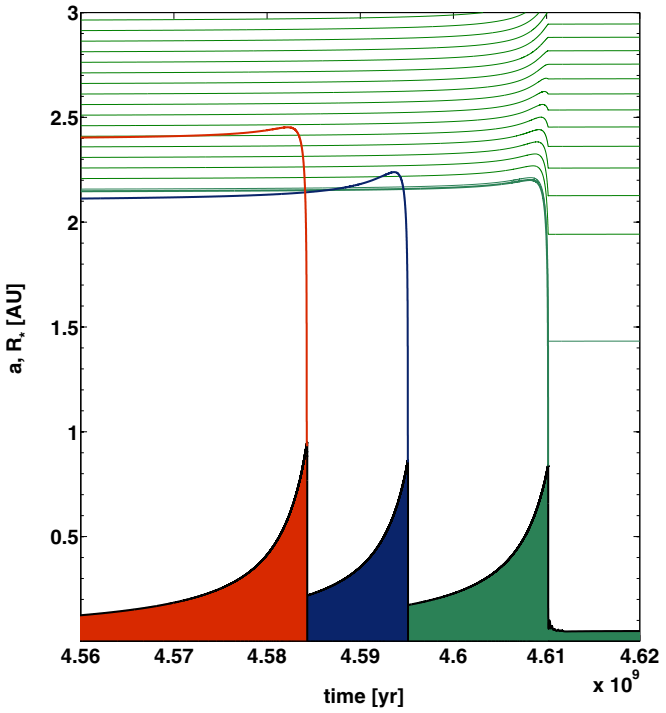

Figure 4. Red ($\eta_R = 0.2$), blue ($\eta_R = 0.5$), and green (Schröder & Cuntz 2005) areas represent the evolution of the stellar radius of a 1.5 $M_\odot$ to the RGB tip. The solid lines are the maximum initial orbital radii for which the planet gets engulfed and are color coded according to the stellar model. For the Schröder & Cuntz (2005) mass-loss prescription model (green), a set of orbits that avoid engulfment are shown.

(A color version of this figure is available in the online journal.)

green for $\eta_R = 0.2$, $\eta_R = 0.5$, and Schröder & Cuntz 2005, respectively) and how this leads to different orbital evolution for a Jupiter-mass planet. The evolution of the maximum initial orbit that enters the stellar envelope is shown for each of the mass-loss prescriptions considered. For the Schröder & Cuntz (2005) model (in green), we also plotted a set of initial orbits representative of the different possible outcomes.

The evolutionary sequences are indistinguishable in terms of the stellar radius during the subgiant phase when mass loss is negligible and the models do not show significant differences (but not when the star starts the ascent on the RGB). Typical values of the radius at the RGB tip are given for the different stellar models in Table 1.

Mass loss influences planet survival due to three combined effects: (1) it modifies the stellar radius, (2) it changes the orbital angular momentum loss efficiency, and (3) it changes the stellar mass and thus its evolutionary timescales. When comparing identical mass-loss prescriptions, if the mass-loss rate is higher (the $\eta_R = 0.5$ case), the pressure on the core is reduced and off-center helium ignition is delayed. The star reaches smaller radii and spends more time on the RGB. Lower mass-loss rates under the same prescription for a given stellar and planet mass lead to more distant planets plunging into the stellar surface due to the combined effects mentioned above. This is why using the lowest mass-loss rate simulation, the one using Reimers with $\eta_R = 0.2$, we obtain the largest critical distance for engulfment (see Figure 4). The impact of mass loss on the stellar properties, however, is a highly nonlinear process that depends on how fast the mass loss accelerates along the RGB. Note the longer resulting RGB evolutionary timescales obtained for the Schröder & Cuntz (2005) model.

The minimum initial orbital distances that a Jupiter-mass planet has to have in order to avoid engulfment are given in the last column of Table 1 for the different stellar models used in the calculation. We obtain critical values for the engulfment radius that are always in the upper envelope of those plotted by Kunitomo et al. (2011) in their figures (for stars $M \geqslant 1.8$–$2\,M_\odot$), but are consistent with those obtained for stars $M \in [1.5$–$1.7]\,M_\odot$. Given the simplification of the tidal forces that these authors made in their paper, we have tried to compute the $a_{\rm crit}$ obtained from their Equation (7) to see if it could be the cause of the difference. We obtain, using this equation, unrealistic critical distances using the numbers provided by our stellar models; the $a_{\rm crit}$ we get under their prescription are very different from the values we obtain with our full calculation. Generally, we find it hard to reproduce the numbers plotted in their graphs.

In their computation of the critical distance, Kunitomo et al. (2011) argued that the differences between the critical distance for engulfment obtained by Villaver & Livio (2009) and their models was due to the inclusion of overshooting. In order to check this assertion, we have computed three models (for $M_\star = 1.5$, 1.7, and $1.9\,M_\odot$) using $\eta_R = 0.5$ and including overshooting with the same prescription as Kunitomo et al. (2011, $\eta_R = 0.5 + OS$ in Table. 1). The critical distances we obtain are similar to the ones obtained in our models without overshooting $\eta_R = 0.5$. We believe that the major differences between ours and the Kunitomo et al. (2011) models are a consequence of having a transition between degenerate and non-degenerate cores at lower stellar masses, and that cannot be attributable only to the inclusion of overshooting in the models.

3.2. Stellar Mass

The stellar mass explicitly enters into the orbital evolution calculations, affecting the relative strength of the different terms

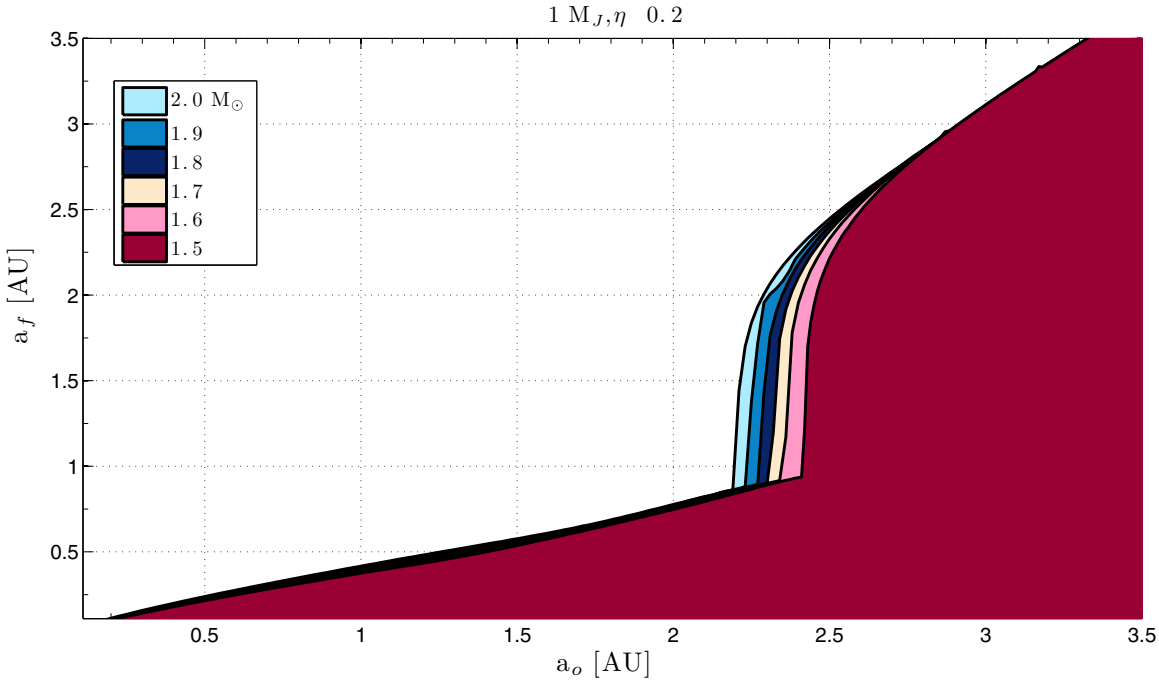

Figure 5. Final (a_f) vs. initial (a_o) orbits reached by a planet of Jupiter mass at the end of the RGB for stellar models with masses between 1.5 and 2 $M_\odot$. The mass-loss prescription adopted for the models shown is that of Reimers, with $\eta_R = 0.2$. The different area colors represent the different stellar masses as indicated in the legend shown in the upper left corner. Planets with final orbits equal to or larger than the initial ones survive the RGB evolution of the star. Planets with initial orbits smaller than that at the inflection point in the curves are engulfed by the stellar envelope. Planets with initial orbits in the narrow range between the inflection point and the 1:1 relation experience tidal decay but remain outside the stellar envelope, as the latter contracted following He-core ignition.

(A color version of this figure is available in the online journal.)

in the angular momentum conservation equations (with the exception of the drag and frictional forces). Furthermore, the mass of the star affects both the evolution of the radius and the maximum radius reached at the end of the RGB. We have quantified the variations in the planet survival distance induced by the stellar mass in Figure 5, where we show the final orbit (a_f) reached by the planet versus the initial one (a_o). This figure is more easily interpreted if compared to Figure 1; the linear part of Figure 5 represents the range of initial orbits that will end up at the stellar surface, the orbits that experience tidal decay but avoid engulfment are those beyond the inflection point in the figure, and, finally, those orbits that experience orbital expansion due to mass loss are those that satisfy $a_f > a_o$. The different colors represent the stellar mass (see the legend at the top left corner of the plot). We have chosen for this plot stellar models with Reimers's mass-loss prescription and the $\eta_R = 0.2$ parameter. All the orbits shown in Figure 5 have been integrated for a Jupiter-mass planet.

Final values of the orbital distance larger than the initial ones imply that a planet initially located at this distance will experience an expansion of the orbit (note that the planets considered are very close to the star and unbinding is not expected; e.g., Villaver & Livio 2007). That is the case for initial orbital distances $a_o \geqslant 2.5$ AU for all masses. Final orbital values smaller than the initial ones have two possible interpretations: (1) the planet has entered the stellar envelope and the final orbit simply reflects the value of the stellar radius (where the calculation is terminated) or (2) the planet has suffered tidal decay, reaching an orbit that avoided the stellar envelope when He-core ignition took place. These two scenarios are well separated in the plot by the inflection point in the curves. The main effect of varying the stellar mass is around the region in the plot where we find orbital decay but the planet avoids the stellar envelope. Note that for initial orbits $a_o < 2.2$ AU there is no difference in the final orbit induced by the stellar mass, but around 2.2 AU $\leqslant a_o \leqslant$ 2.5 AU increasing the stellar mass leads to larger final orbital distances which translates into more chances for planet survival.

A larger stellar mass decreases the influence of the mass-loss term (and its tendency to move the orbit outward) and decreases the strength of the tidal forces, effects that operate in opposite directions for planet survival (see Equation (3)). Figure 5 shows that the stellar mass has a stronger influence through the tidal term than through the mass-loss term. This is reflected by the larger distances from the star cleared of planets (smaller color areas in Figure 5) as a result of the evolution of stars with lower masses. Note also that we have chosen the least favorable scenarios, the models with the smallest mass-loss rates, to show this effect. The larger the area shown beyond the inflection point, the better the chances for planet survival.

3.3. Planet Mass

The dependency of planet survival on the RGB as a function of the planet mass using Neptunian and 1, 2, 5, and 10 M$_J$ (Jupiter Mass) planets is shown in Figure 6 for a 2 $M_\odot$ star with Reimers mass loss and $\eta_R = 0.2$. As already noted in VL09, for a low-mass planet to be engulfed, its initial separation needs to be smaller than that of a more massive planet. This is because, at an equal initial separation from the star, a more massive companion exerts a stronger tidal torque (due to the dependency on q in Equation (7)). Note that the effect of the planet's mass is negligible in the mass-loss term. Overall, survival is easier for smaller mass planets around RGB stars since they experience weaker tidal forces. Figure 6 demonstrates that planet survival is quite sensitively dependent on the planet's mass.

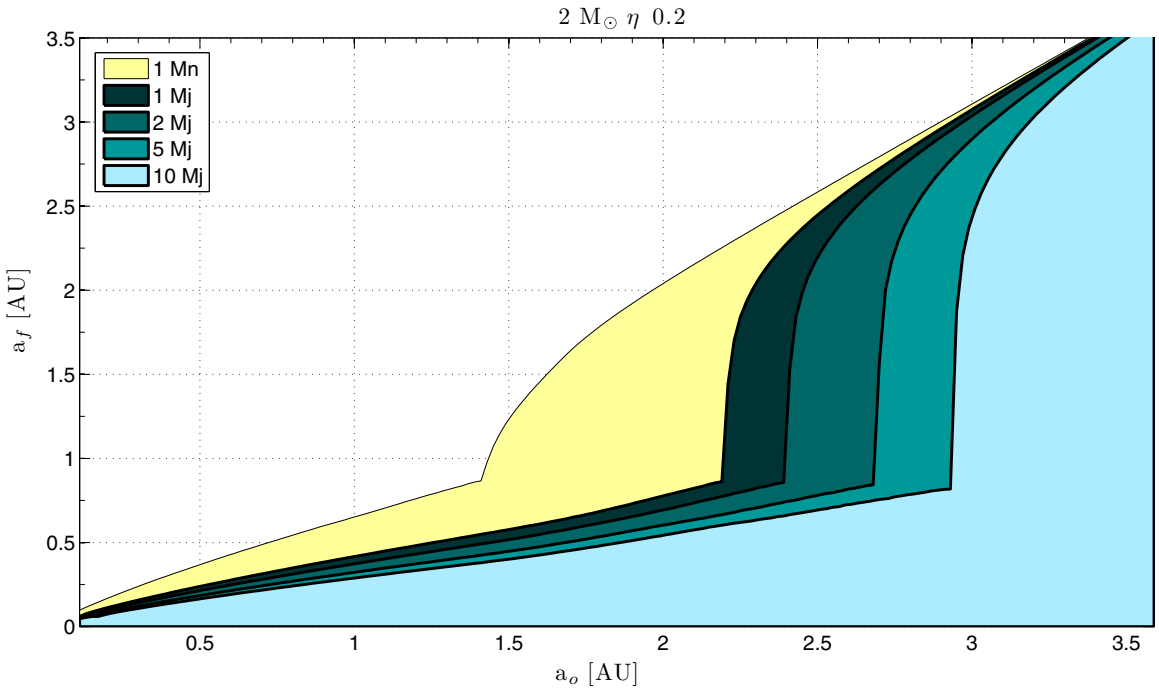

Figure 6. Same as Figure 5, but using a star with 2 $M_{\odot}$, Reimer's mass loss with $\eta_R = 0.2$, and varying the planet mass between Neptune mass (1 M_N in the legend in the top left corner) and 1, 2, 5, and 10 Jovian masses (10 M_J; light blue area).

(A color version of this figure is available in the online journal.)

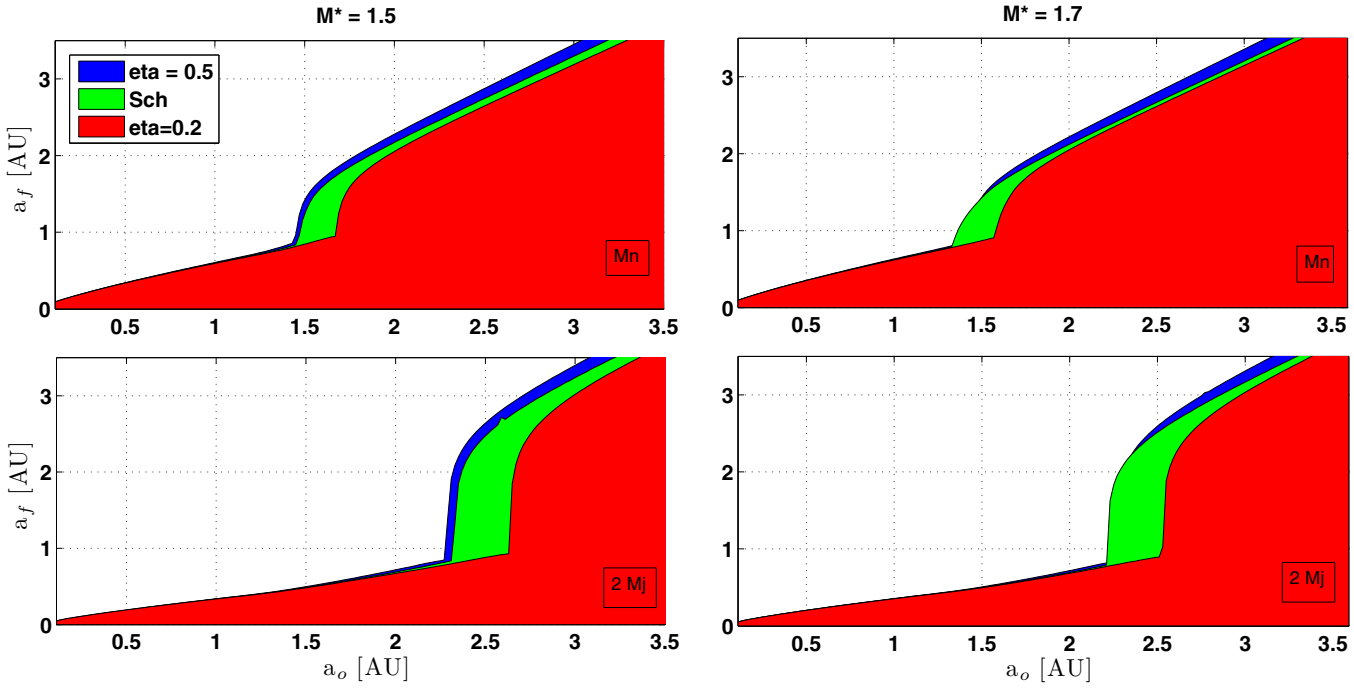

Figure 7. Left column: variation under the mass-loss prescriptions used in the stellar evolution calculations of the final (a_f) vs. initial (a_o) orbits of a planet orbiting a 1.5 $M_{\odot}$ star. The top panels are for a planet with Neptune mass and the bottom plots are for planets with twice the mass of Jupiter. Right column: the same but for a star with 1.7 $M_{\odot}$. The legend in the top left corner gives the mass-loss prescriptions used in the calculation of the stellar structure. The mass of the star is indicated at the top of each column and the planet mass at the bottom right corner of each plot.

(A color version of this figure is available in the online journal.)

Note that the case of massive companions that can tidally transfer enough angular momentum to the star and significantly spin up the primary (Garcia-Segura et al. 2014) has not been considered. In such cases, enhanced mass loss and deformation of the primary might take place as well. Nordhaus & Spiegel (2013) estimated that this behavior starts to be important for $M_c/M_* > 0.1$, with M_c the mass of the companion, and excluded this region of parameter space from their calculations. Note that the largest M_c/M_* we use is 6×10^{-3}, well under the Nordhaus & Spiegel (2013) estimated limit.

In Figure 7, we show a sample of the computations to demonstrate the various effects. The left and right columns

show the effects of varying the stellar mass with different planet masses, represented in the top and bottom panels of each column. Within each plot, the different mass-loss prescriptions used are shown using different colors. This figure summarizes our findings: (1) that planet survival depends strongly on the planet mass and (2) that the effects of varying the planet mass dominate over changes in the mass-loss prescriptions or the stellar mass in the range considered.

Observational determination of planetary masses through the radial velocity technique carries the uncertainty of an unknown inclination angle of the orbit, and thus only minimum planet masses are available. Uncertainties in stellar masses also contribute to uncertainties in the planet mass determinations. We show that the largest uncertainties in the outcome of the process of planet survival along the RGB might be associated with the uncertainties in the planet masses and not to uncertainties in the stellar mass determination or the mass-loss prescription used in the models.

3.4. Eccentricity Evolution

In order to consider a planet's eccentricity variations, we integrate Equations (3–16). For the eccentricity study, we have chosen two values of the mass of the planet (1 M_J, 1 M_N), two stellar masses (1.5, 2 $M_\odot$), and $\eta_R = 0.5$. Note that mass loss has little effect on the planet's eccentricity, since the mass-loss rates are rather small and the orbits considered here are relatively close to the star (e.g., Veras et al. 2011). The planet's spin rate was in all cases initially 100 rad/yr, but we verified that the exact initial value is unimportant.

The planet's radius was fixed at 1 Jupiter radius (1 R_J) or 1 M_N for the Neptune-mass planet; we did not consider the planet's radius expansion due to tidal energy being deposited in the planet's interior. The planetary tidal strength was set to $Q'_{\rm pl} = 10^5$ and the stellar properties were evolved using the models as described in Section 2.1 from the pre-MS. As before, the star in our models does not spin.

As noted above, for the study of the eccentricity evolution, we kept the planet's radius, $R_{\rm p}$, fixed in Equations (10)–(12). In real systems, the heating of a planet's interior by tidal forces can cause the planet to expand, further strengthening tidal forces and potentially even leading to a runaway process. This effect, important to consider in detailed studies of the evolution of MS close-in planets, would have little importance in the overall outcome of the systems considered in this paper: if they are close enough for substantial tidal heating, they would have been engulfed very early by the expansion of the star. Furthermore, for simplicity, we have removed from Equation (3) the second term involving the frictional and gravitational drag forces since we have seen in the previous part of the study that they have a negligible effect in reducing the semimajor axis over the RGB lifetime.

Some comments on the qualitative behavior of the effects of stellar and planetary tides are in order. The evolution of the eccentricity on the MS, when the stellar radius is small, is dominated by planetary tides (e.g., Matsumura et al. 2010). During that period, the planet is rapidly brought into a state of pseudosynchronization, where

$$\Omega_{\rm pl} = \frac{g_2}{g_5(1-e^2)^{3/2}} n. \quad (17)$$

Once this is attained, the planet's eccentricity decays while preserving the orbit's angular momentum, following a trajectory in the $a-e$ space

$$e = \sqrt{1 - a_f/a}. \quad (18)$$

Here, the eccentricity decays to zero as the semimajor axis decays to a finite value, a_f. In contrast, when the stellar radius is much larger, stellar tides dominate the evolution on the RGB. Neglecting frequency dependencies for simplicity, the planet's orbit follows a trajectory,

$$e = e_0 \left(\frac{a}{a_f}\right)^{9/2}, \quad (19)$$

where e_0 is the initial eccentricity. Now the eccentricity decays to zero as the semimajor axis decays to zero. This qualitatively different behavior of the $a-e$ trajectories under stellar and planetary tides has important implications for the shape of the $a-e$ envelope, as discussed later.

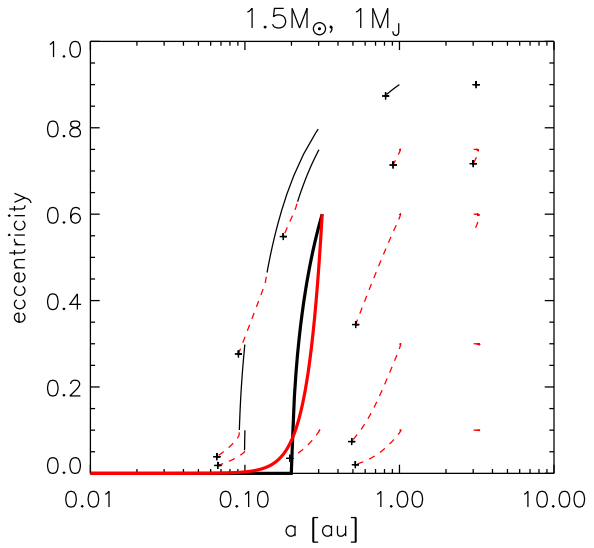

Figure 8. Sample evolutionary tracks in $a-e$ space of planets of mass 1 M_J orbiting a 1.5 $M_\odot$ star. Line styles show different evolutionary phases: the solid black line is the MS and the dashed line the RGB. Crosses indicate where planets are engulfed by the star. The solid and red thick lines show the analytical approximation of the evolution on the MS and RGB, respectively (Equations (16) and (17)).

(A color version of this figure is available in the online journal.)

In Figure 8, we show samples of the evolution of a 1 M_J planet on the $a-e$ plane. Evolution on the stellar MS is shown as black solid lines and on the RGB as red dashed lines. On the MS, the planet's path is determined by planetary tides and it follows Equation (18), which brings the eccentricity down steeply while typically causing a modest decay in semimajor axis. An illustration of this path is shown in Figure 8 as a thick black line. On the RGB, however, stellar tides dominate and the track follows a shallower path as a and e decay at similar rates (see the red solid thick line). The difference in the tracks is most clearly seen in the planets starting at 0.1 AU in Figure 8. Very distant planets do not experience tides and their orbits expand due to mass loss. Planets at intermediate distances at around 1 AU execute a hook, as they first see their orbits expand due to mass loss but then decay tidally as the stellar radius grows. Most of the planets plotted in Figure 8 are eventually engulfed on the RGB.

Populations of planets in the $a-e$ plane are shown in Figure 9. To make this plot, we filled the region $a \in [0.01, 10]$ AU and $e \in [0, 0.95]$ (with e increasing in steps of 0.05) with 2964 planets and let the star and the orbit evolve.

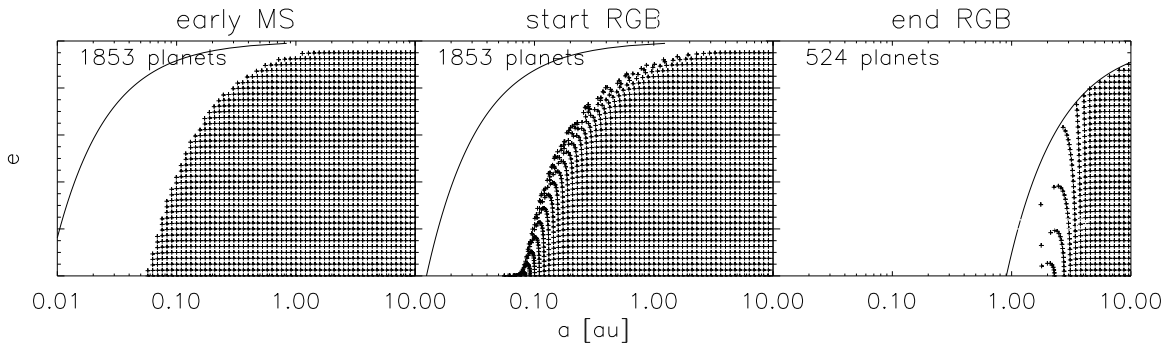

Figure 9. Populations of 1 M_J planets orbiting 1.5 $M_\odot$ stars at three points in the star's life: early MS (left) ≈20 Myr, beginning of RGB (center), and end of RGB (right). The solid line marks the locus where the planets' pericenters lie on the stellar surface. The number of planets is shown in each panel.

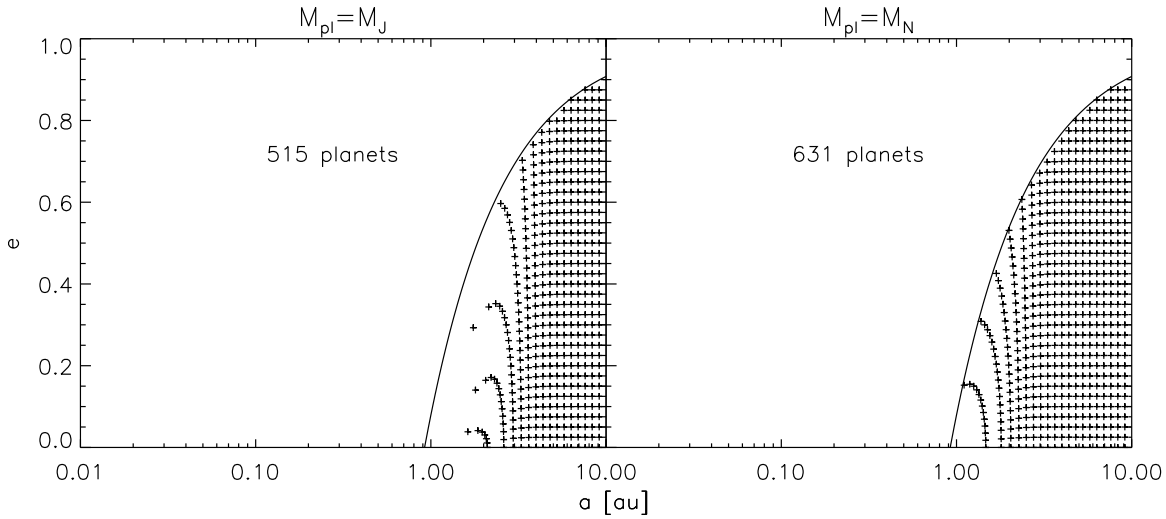

Figure 10. Effects of changing the planet mass on the planet population surviving the RGB. Left to right: 2 $M_\odot$ and 1 M_J; 2 $M_\odot$ and 1 M_N.

Planets with pericenters inside the stellar envelope at any time are then removed. We show the populations at meaningful times in the star's life: very early in the MS (at ≈20 Myr), to show the set of initial conditions being integrated, i.e., those that did not have their pericenters inside the stellar envelope during pre-MS contraction; at the start of the RGB (defined by $R_\star = 3.4\,R_\odot$), showing the extent of eccentricity decay during the MS, largely due to planetary tides; and at the end of the RGB, showing the clearing effects of stellar tides and the expanded stellar envelope. We included the star's pre-MS contraction phase in the calculation, which limited the initial pericenters of our planet population (note that we run models for the $a-e$ parameter space described above). By following the pre-MS and MS evolution, the goal was not to study those phases in detail but rather to get some reasonably realistic initial conditions for the post-MS phase. Note that while the envelope expands to only ∼1 AU, the region out to 2–3 AU shows significant depletion of the planetary population.

Figure 10 shows the effects of varying the planetary mass on the distribution of orbital properties at the end of the RGB. As we have previously discussed, we see a larger initial region of orbital distances, resulting in the number of planets getting accreted onto the stellar surface increasing as the planet mass increases. In general, we find that on the RGB, very eccentric and distant planets ($a \gtrsim 3$ AU, $e \gtrsim 0.8$) do not see much eccentricity decay, and their engulfment is basically just determined by their pericenter location and the maximum stellar radius.

Finally, in Figure11, we show how stellar tidal forces on the early RGB can create a transient population of moderately eccentric close-in Jovian planets. In Figure 11, the envelope for "start RGB" is defined such that there are no planets lying above the envelope at the initial RGB output timestep. The envelope for "all RGB" is defined such that there are no planets lying above the envelope at any RGB output timestep, i.e., at no point on the RGB is a planet found above the envelope. For every point below the envelope, there exists at least one time, t, such that a planet is found there.

Eccentric planets with $a \lesssim 0.05$ AU are depleted on the MS due to the action of planetary tides. However, as discussed above, planetary and stellar tidal forces cause planets to follow different tracks in the $a-e$ plane. Once the stellar radius begins to increase on the RGB, stellar tidal forces begin to dominate over planetary tidal forces, and the planets now follow tracks through the region depleted on the MS, with $a \sim 0.05$ AU and $e \sim 0.2$. Planets following these tracks, however, are rapidly engulfed by the expanding stellar envelope. Neptune-mass planets do not exhibit this behavior, since the stellar tides they excite are much weaker.

4. DISCUSSION

The semimajor axis distribution of planets discovered with radial velocity surveys as of 2013 September 1[5] is plotted versus the stellar mass in Figure 12. The points have been color coded according to the evolutionary status of the star, with dark blue,

[5] Data from exoplanet.eu, exoplanets.org (Schneider et al. 2011; Wright et al. 2011).

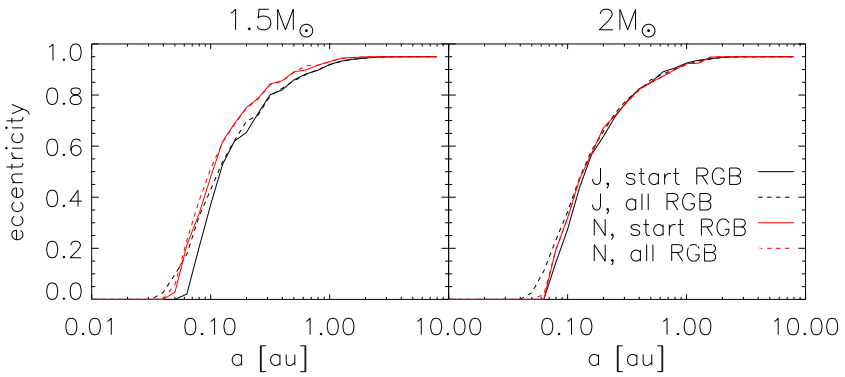

Figure 11. Envelopes of planet populations around 1.5 $M_{\odot}$ and 2 $M_{\odot}$ stars (left and right panels, respectively). Envelopes of the population at the beginning of the RGB are shown as solid lines, while envelopes over the *whole* RGB population are shown as dashed lines. Stellar tides cause some Jovian planets to decay through a region of moderate eccentricity and small semimajor axis that was depleted during MS evolution by planetary tides.

(A color version of this figure is available in the online journal.)

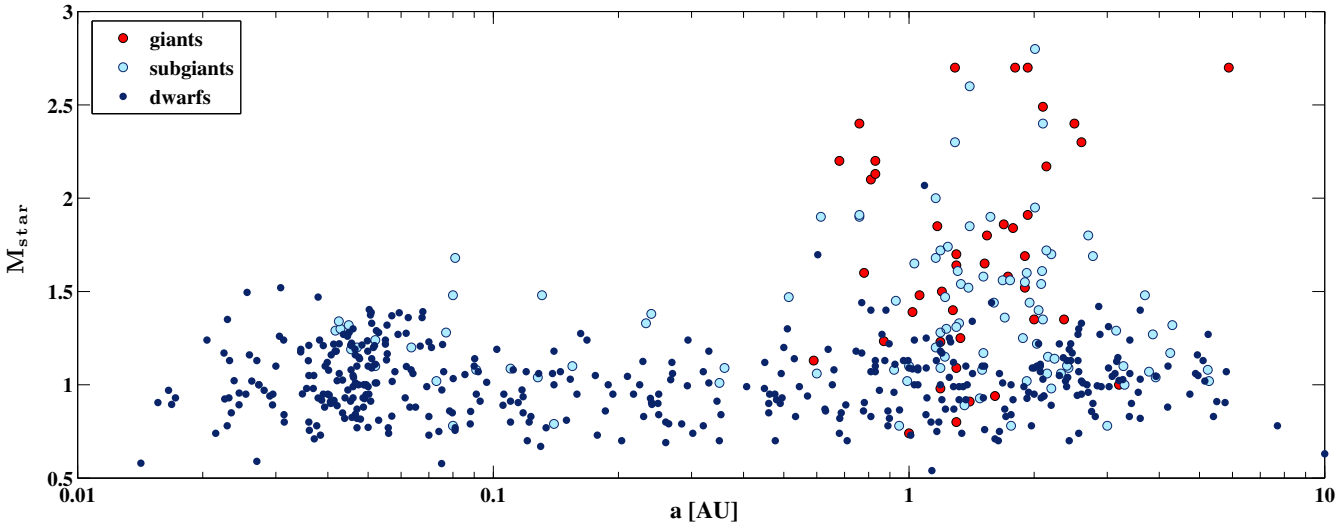

Figure 12. Observed orbital distance vs. the stellar mass of all the confirmed planets detected through the radial velocity method taken from the Exoplanet encyclopedia (exoplanet.eu, exoplanets.org). The different colors represent the evolutionary status of the star as determined by the published luminosity class.

(A color version of this figure is available in the online journal.)

light blue, and red representing MS, subgiant, and red giant stars, respectively.

The planet population orbiting massive host stars (meaning $M \geqslant 1.5\ M_{\odot}$) has been claimed to be distinct with respect to the minimum orbital distances at which planets are found (see, e.g., Johnson et al. 2010; Sato et al. 2008; Bowler et al. 2010). Indeed, no planet around a giant has been found so far with $a < 0.54$ AU[6] (from radial velocity measurements). This fact (taken alone) has been used to suggest a relation between planet formation and stellar mass (Currie 2009). However, as we see in Figure 12, planets orbiting subgiant stars populate the region $a \leqslant 0.54$ AU and can be found as close as 0.08 AU orbiting the subgiant star HD 102956 (Johnson et al. 2010). Furthermore, recent transit surveys have discovered hot Jupiters around MS A–F stars that remained elusive for radial velocity surveys (e.g., HAT-P-49, Bieryla et al. 2014; WTS-1b, Cappetta et al. 2012; Kepler-14b, Buchhave et al. 2011; WASP-33, Collier Cameron et al. 2010; KELT-3b, Pepper et al. 2013; COGLE-TR-L9, Snellen et al. 2009). These are all mostly fairly low-mass stars (1.5, 1.2, 1.5, 1.5, 1.3, and 1.5 $M_{\odot}$). The best example so far of a close-in planet around a high-mass star is HD 102956b orbiting a 1.7 $M_{\odot}$ star (Johnson et al. 2010). A transiting planet, Kepler-91b has been found at 0.072 AU from the star (Lillo-Box et al. 2014a) as well, holding the record for the innermost planet found around an RGB star. However, note that that the stellar mass is 1.3 $M_{\odot}$, a relatively low value compared to most RGB planet host stars, and recent claims have been made of a false positive for this system (Sliski & Kipping 2014; Esteves et al. 2013). Note that the planet has now been confirmed using an independent method (Lillo-Box et al. 2014b).

If close-in planets are present in the MS stage orbiting A-F stars, but not found in radial velocity searches around evolved stars, this suggests that it is the evolution of the star, and not its mass, that plays a role in removing planets from close orbits. In fact, as we have shown here, close-in planets enter the stellar envelope as the star leaves the MS and evolves onto the RGB (see also Villaver & Livio 2009; Kunitomo et al. 2011). As the star evolves, it removes planets from a region that extends far beyond the stellar radius to the entire region of tidal influence ($a/R_{*} \approx$ 2–3; see Figure 13 for a Jupiter-mass planet). The star first, during the subgiant phase, clears out the very close-in planets present during the MS evolution and then proceeds to clear out a larger region as the stellar radius increases

[6] The planets orbiting BD+15 2940 at 0.54 AU (Nowak et al. 2013), HIP 63242 at 0.57 AU (Jones et al. 2014) hold the record.

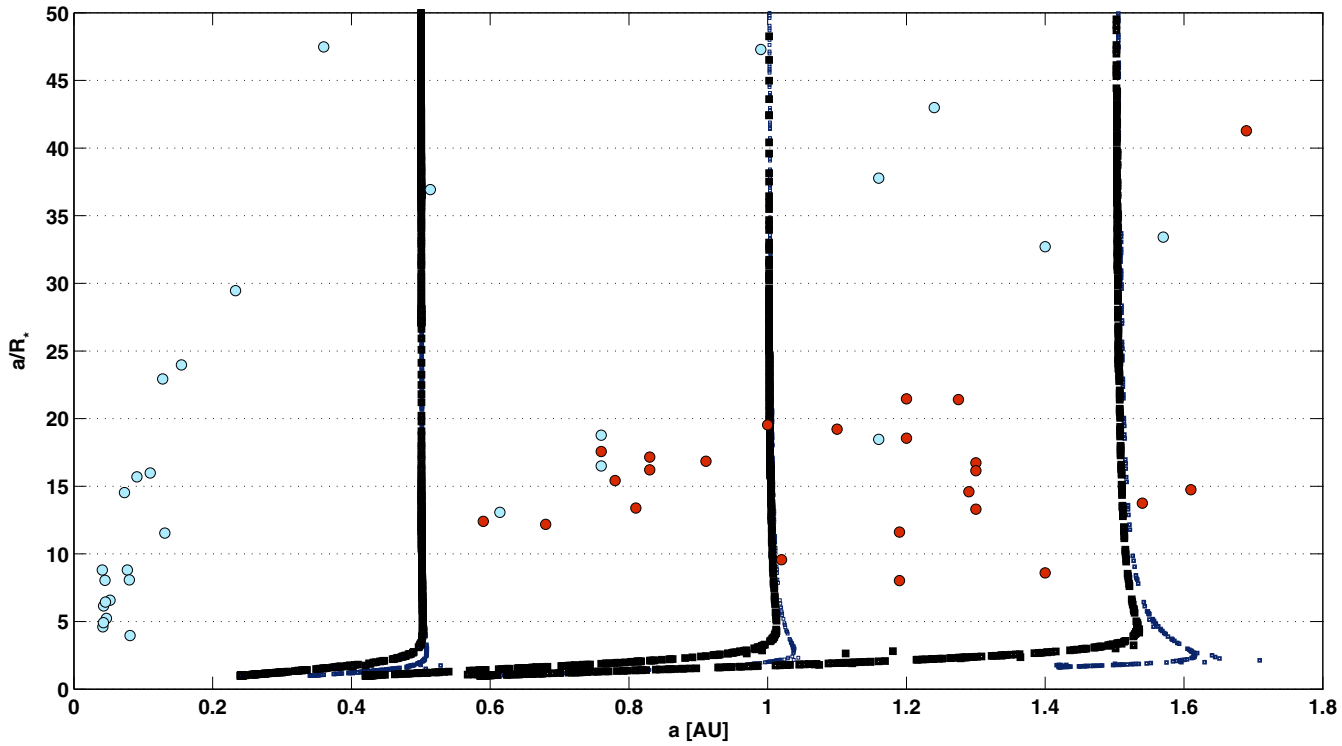

Figure 13. Ratio of the orbital distance to the stellar radius vs. the orbital distance of the observed population of planets orbiting subgiant stars (light blue points) and giant stars (red points). The evolution of the orbital to stellar ratio is shown for three initial orbital distances (0.5, 1, and 1.5 AU) and two stellar masses, 1.5 $M_{\odot}$ (in dark blue) and 2 $M_{\odot}$ (in black), and a Jupiter-mass planet.

(A color version of this figure is available in the online journal.)

when it ascends the RGB. The tidal influence region is where planets are expected to be depleted from as the star evolves. Note in Figure 13 that most observed planets are safe from being engulfed since they are located far beyond this region. Theoretical predictions agree with the observations since there is just one planet detection with $a/R_{*} \leqslant 2.5$ (the closest one, Kepler-91b, has $a/R_{*} \approx 2.45$; Lillo-Box et al. 2014a).

A feature that is harder to understand in Figure 12 is the absence of planets in the upper middle region in the plot (no planets found around subgiant stars with $0.08 \leqslant a_o \leqslant 0.5$ AU) and $M \geqslant 1.5\,M_{\odot}$. Planets are found close to massive subgiant stars and around them beyond 0.5 AU, but no subgiant with $M \geqslant 1.5\,M_{\odot}$ has been found with planets in that narrow range of orbits. Planets are not expected to be cleared out that far by tides during the evolution of the star along the subgiant phase. These planets are expected to be engulfed by the star later on, during the RGB evolution. So the question is, why are there planets found in the $0.08 \leqslant a_o \leqslant 0.5$ AU orbital range around less massive subgiants but not around subgiants with $M \geqslant 1.5\,M_{\odot}$?

In this paper, we have explored a host mass range between 1.5 and 2 $M_{\odot}$ for planet survival. Within this mass range, we find that during the subgiant phase planet survival is not substantially affected either by the stellar mass, or the mass-loss prescription adopted in the calculation within the reasonable assumptions adopted for the stellar models. The main parameter affecting planet survival during the subgiant phase is the planet mass. More massive planets are more likely to plunge into the stellar envelope earlier. More massive planets are formed preferentially in more massive protoplanetary disks, and thus those planets are expected around more massive stars. If more massive planets are present around subgiants with $M \geqslant 1.5\,M_{\odot}$, then they could be brought into the stellar envelope early in the evolution if they are initially located at a relatively close distance from the star, and this could explain why they are not found in the $0.08 \leqslant a_o \leqslant 0.5$ AU orbital range. Less massive planets are harder to detect around these systems. There is an observational bias associated with the large stellar jitter in evolved hosts that prevents the detection of low-mass planets around evolved stars. In fact, more massive planets are found on average orbiting evolved stars (which, in principle, are more massive than the average MS planet hosts). The lack of observed planets around subgiants with $M \geqslant 1.5\,M_{\odot}$ in the $0.08 \leqslant a_o \leqslant 0.5$ AU orbital range is hard to understand otherwise from a theoretical perspective.

The RGB evolution is short compared to the MS lifetime, implying that the RGB region in the H-R diagram is populated by stars of similar mass (for a given initial chemical composition and age). Masses for RGB (planet-hosting) stars are computed from spectroscopic values of $T_{\rm eff}$ and metallicities that together with visual magnitude estimates are used to interpolate in theoretical stellar evolution grids. The uncertainties involved in the measured parameters are therefore relatively large. Furthermore, the tracks for the different masses in the H-R diagram are packed together and, as a consequence, estimates of masses for RGB stars carry large uncertainties. Uncertainties in mass are for the most part $\leqslant$0.1 ($\leqslant$10%; see, e.g., Maldonado et al. 2013; Mortier et al. 2013; Zieliński et al. 2012), with some objects having larger uncertainties (up to 0.3) mostly caused by the lack of available *Hipparcos* parallaxes (van Leeuwen 2007). The stellar radii have the same dominant source for the uncertainty as the stellar masses and have values of ≈6%–15%. We have shown that mass differences within the studied range do

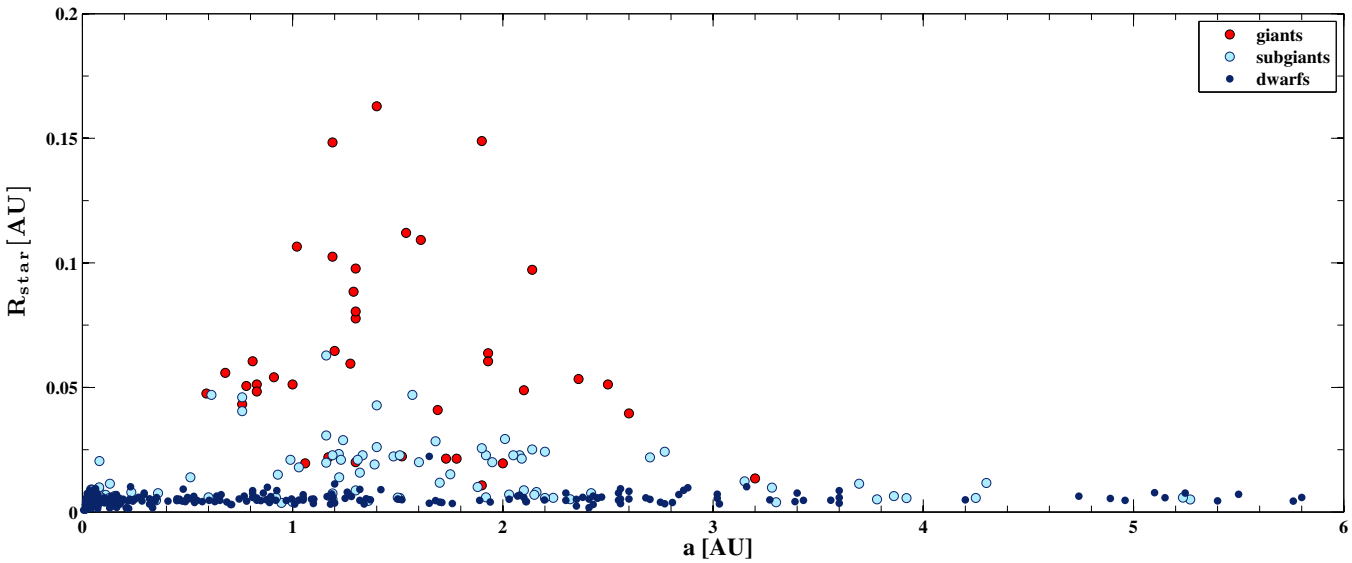

Figure 14. Same as Figure 12, but here the observed orbital distance is plotted against the stellar radius.
(A color version of this figure is available in the online journal.)

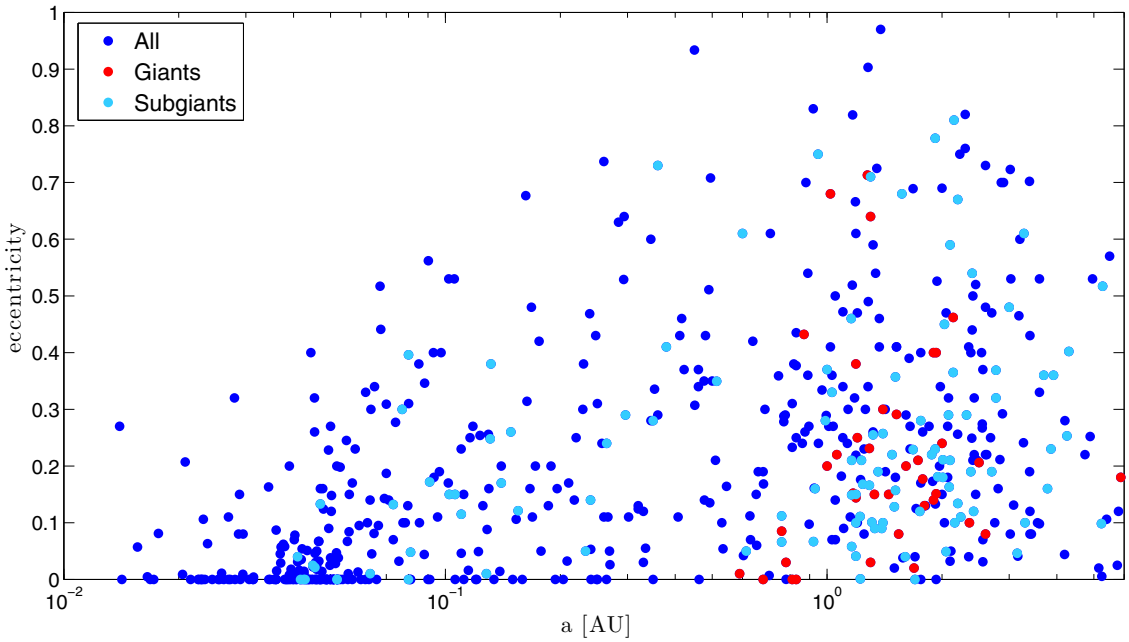

Figure 15. Same as Figure 12, but here the observed planet eccentricity is plotted vs. orbital distance.
(A color version of this figure is available in the online journal.)

not have a strong influence on planet survival along the RGB, and thus observed mass uncertainties should not have a strong influence on the outcome of the distribution of observed planets.

It has been argued that the planet survival limit is rather sensitive to the host star's mass (Kunitomo et al. 2011). While this is true when the stellar mass crosses from low to intermediate mass (where the stellar core conditions change from degenerate to not degenerate), it is not true when low-mass stars are involved. Along these lines, it is important to remember that while the RGB $T_{\rm eff}$ at a given luminosity is only slightly sensitive to the value of the stellar mass, it is affected by the initial value of the metallicity Z. Increasing Z moves the transition between low- and intermediate-mass stars toward higher masses. Higher mass stars would ascend the RGB faster and grow smaller in radius (note that this transition mass is set at 1.4 $M_{\odot}$ in Lloyd 2013, where he argues for a lower-mass planet hosting evolved stars than claimed in the literature). Our limit for He-flash stars is 2.5 $M_{\odot}$ for [Fe/H] = 0.19. It is the mass limit between degenerate and non-degenerate cores that strongly influences the planet survival limit during the RGB. Close-in planets thus would have more chances to survive orbiting metal-poor stars due to this effect. Note that the mass limit to build a degenerate core along the RGB is 1.5 $M_{\odot}$ for $Z = 0.01 Z_{\odot}$ (Sweigart et al. 1990).

We have shown that for a given mass-loss prescription, increasing the stellar mass puts more planets into the safe zone limit. This is because the stellar mass has a stronger influence (through the tidal term) than the mass-loss term.

In Figure 14, we show the distribution of stellar radii as a function of orbital separation for planets found in radial velocity

surveys. The planets clearly occupy different regions according to the evolutionary status of the star. In this plot, the striking feature is the lack of planetary systems found orbiting giant stars at large distances, beyond 3 AU. There is nothing in principle that could cause this region to be depleted of planets unless stellar jitter is preventing detection at large distances or planet searches around giant stars have not been carried long enough to recover this planet population present, on the other hand, around MS stars. We find that all the observed systems are within the a/R_* safe zone from tidal interaction, which we find from the calculation of the orbital evolution.

Regarding the eccentricities of planet orbits, the observed distribution is shown in Figure 15. According to theoretical expectations, giant stars, being systems dominated by stellar tides, tend to have a and e decaying at similar rates. It is expected therefore that planets experiencing tidal eccentricity decay would also experience orbital decay, and thus would not be observed. Subgiants and MS stars, on the other hand, could have experienced eccentricity decay but not substantial orbital decay, explaining the upper left corner clearance zone in the plot.

In summary, our calculations show that rapid tidal orbital decay occurs when $a/R_* < 3$. There are only three planets found orbiting RGB stars with $a/R_* < 10$, and none has been found with $a/R_* < 8$. The region $\in$[0.08, 0.5] AU around subgiants is too wide to have been depleted of planets just by tidal effects, so the depletion must have other origins and cannot be primordial since these planets have been found recently orbiting A-F MS stars using imaging techniques. A mass-dependent mechanism must be at play that can only act in one way, by building more massive planets that are around more massive hosts and, due to tidal forces, are brought into the stellar envelope from larger initial orbital distances. The only way that makes sense is if the RGB stars indeed have higher masses, distinct from the MS planet hosts. If the RGB stars have low masses, as Lloyd (2013) and Schlaufman & Winn (2013) argue, then there is no sensible way to account for the lack of close-in RGB planets, since the stellar radius is too small to cause depletion by tidal forces (unless the stellar radii are systematically underestimated, by a factor of three or more).

5. CONCLUSIONS

In this work, we have quantified the influence of different parameters on the survival of planets orbiting subgiant and red giant stars. We have explored a mass range for the hosts between 1.5 and 2 $M_\odot$ and find that during the subgiant phase, planet survival is not substantially affected either by the stellar mass or the adopted mass-loss prescription. The main parameter affecting planet survival during the subgiant phase is the planet mass, with more massive planets being more likely to plunge into the stellar envelope earlier.

We find that even though the observed uncertainties in the determination of the stellar mass or mass-loss rates are quite large, they do not have much influence on the critical orbit beyond which a planet will survive RGB evolution. Since tidal torques drop as a high negative power of the ratio of stellar radius to orbital separation, companions that escape engulfment experience essentially no tidal interactions if they are located beyond a certain initial orbit. Planets located at $a/R_* \approx 2$–3 are in jeopardy as soon as the star leaves the MS, since that is where the tidal force starts to dominate the orbital evolution.

Eccentric planets with $a \lesssim 0.05$ AU are depleted on the MS due to the action of planetary tides. However, once the stellar radius begins to increase on the RGB, stellar tidal forces begin to dominate over planetary tidal forces, and planets follow tracks through the region depleted on the MS, with $a \sim 0.05$ AU and $e \sim 0.2$. Planets following these tracks, however, are rapidly swallowed by the expanding stellar envelope. Also important is that we find that during the RGB, very eccentric and distant planets do not experience much eccentricity decay, and that planet engulfment is basically just determined by the pericenter location and the maximum stellar radius.

The work of E.V. and A.J.M. was supported by the Spanish Ministerio de Ciencia e Innovación (MICINN), Plan Nacional de Astronomía y Astrofísica, under grant AYA2010-20630 and by the Marie Curie program under grant FP7-People-RG268111. L.S. is an FNRS research associate. We thank Amy Bonsor for useful discussions.

REFERENCES

Adams, F. C., & Bloch, A. M. 2013, ApJL, 777, L30
Alexander, M. E., Chau, W. Y., & Henriksen, R. N. 1976, ApJ, 204, 879
Bear, E., & Soker, N. 2011, MNRAS, 411, 1792
Bieryla, A., Hartman, J. D., Bakos, G. A., et al. 2014, AJ, 147, 84
Bowler, B. P., Johnson, J. A., Marcy, G. W., et al. 2010, ApJ, 709, 396
Buchhave, L. A., Latham, D. W., Carter, J. A., et al. 2011, ApJS, 197, 3
Cappetta, M., Saglia, R. P., Birkby, J. L., et al. 2012, MNRAS, 427, 1877
Carlberg, J. K., Majewski, S. R., Patterson, R. J., et al. 2011, ApJ, 732, 39
Charpinet, S., Fontaine, G., Brassard, P., et al. 2011, Natur, 480, 496
Collier Cameron, A., Guenther, E., Smalley, B., et al. 2010, MNRAS, 407, 507
Currie, T. 2009, ApJL, 694, L171
Debes, J. H., & Sigurdsson, S. 2002, ApJ, 572, 556
de Medeiros, J. R., Da Rocha, C., & Mayor, M. 1996, A&A, 314, 499
Dobbs-Dixon, I., Lin, D. N. C., & Mardling, R. A. 2004, ApJ, 610, 464
Duncan, M. J., & Lissauer, J. J. 1998, Icar, 134, 303
Esteves, L. J., De Mooij, E. J. W., & Jayawardhana, R. 2013, ApJ, 772, 51
Garcia-Segura, G., Villaver, E., Langer, N., Yoon, S.-C., & Manchado, A. 2014, ApJ, 783, 74
Goldreich, P., & Nicholson, P. D. 1977, Icar, 30, 301
Grevesse, N., Noels, A., & Sauval, A. J. 1996, in ASP Conf. Ser. 99, Standard Abundances, ed. S. S. Holt & G. Sonneborn (San Francisco, CA: ASP), 117
Iben, I., Jr. 1967, ARA&A, 5, 571
Jackson, B., Barnes, R., & Greenberg, R. 2009, ApJ, 698, 1357
Jackson, B., Greenberg, R., & Barnes, R. 2008a, ApJ, 678, 1396
Jackson, B., Greenberg, R., & Barnes, R. 2008b, ApJ, 681, 1631
Johnson, J. A., Bowler, B. P., Howard, A. W., et al. 2010, ApJL, 721, L153
Johnson, J. A., Butler, R. P., Marcy, G. W., et al. 2007, ApJ, 670, 833
Johnson, J. A., Morton, T. D., & Wright, J. T. 2013, ApJ, 763, 53
Jones, M. I., Jenkins, J. S., Bluhm, P, Rojo, P., & Melo, C. H. F. 2014, A&A, 566, A113
Kratter, K. M., & Perets, H. B. 2012, ApJ, 753, 91
Kunitomo, M., Ikoma, M., Sato, B., Katsuta, Y., & Ida, S. 2011, ApJ, 737, 66
Lillo-Box, J., Barrado, D., Henning, Th., et al. 2014b, A&A, 568, L1
Lillo-Box, J., Barrado, D., Moya, A., et al. 2014a, A&A, 562, A109
Livio, M., & Soker, N. 1984, MNRAS, 208, 763
Livio, M., & Soker, N. 1988, ApJ, 329, 764
Lloyd, J. P. 2013, ApJL, 774, L2
Lovis, C., & Mayor, M. 2007, A&A, 472, 657
Maldonado, J., Villaver, E., & Eiroa, C. 2013, A&A, 554, A84
Massarotti, A., Latham, D. W., Stefanik, R. P., & Fogel, J. 2008, AJ, 135, 209
Matsumura, S., Peale, S. J., & Rasio, F. A. 2010, ApJ, 725, 1995
Moeckel, N., & Veras, D. 2012, MNRAS, 422, 831
Mortier, A., Santos, N. C., Sousa, S. G., et al. 2013, A&A, 557, A70
Mustill, A. J., & Villaver, E. 2012, ApJ, 761, 121
Niedzielski, A., Goździewski, K., Wolszczan, A., et al. 2009, ApJ, 693, 276
Nordhaus, J., & Blackman, E. G. 2006, MNRAS, 370, 2004
Nordhaus, J., & Spiegel, D. S. 2013, MNRAS, 432, 500
Nordhaus, J., Spiegel, D. S., Ibgui, L., Goodman, J., & Burrows, A. 2010, MNRAS, 408, 631
Nowak, G., Niedzielski, A., Wolszczan, A., Adamów, M., & Maciejewski, G. 2013, ApJ, 770, 53
Ogilvie, G. I. 2014, arXiv:1406.2207
Ogilvie, G. I., & Lesur, G. 2012, MNRAS, 422, 1975

Ostriker, E. C. 1999, ApJ, 513, 252
Passy, J.-C., Mac Low, M.-M., & De Marco, O. 2012, ApJL, 759, L30
Penev, K., & Sasselov, D. 2011, ApJ, 731, 67
Penev, K., Sasselov, D., Robinson, F., & Demarque, P. 2007, ApJ, 655, 1166
Pepper, J., Siverd, R. J., Beatty, T. G., et al. 2013, ApJ, 773, 64
Rasio, F. A., Tout, C. A., Lubow, S. H., & Livio, M. 1996, ApJ, 470, 1187
Reimers, D. 1975, MSRSL, 8, 369
Rosenhead, L. (ed.) 1963, Laminar Boundary Layer (Oxford: Clarendon Press)
Sato, B., Izumiura, H., Toyota, E., et al. 2007, ApJ, 661, 527
Sato, B., Izumiura, H., Toyota, E., et al. 2008, PASJ, 60, 539
Schlaufman, K. C., & Winn, J. N. 2013, ApJ, 772, 143
Schneider, J., Dedieu, C., Le Sidaner, P., Savalle, R., & Zolotukhin, I. 2011, A&A, 532, A79
Schröder, K.-P., & Cuntz, M. 2005, ApJL, 630, L73
Siess, L. 2006, A&A, 448, 717
Siess, L., & Livio, M. 1999a, MNRAS, 304, 925
Siess, L., & Livio, M. 1999b, MNRAS, 308, 1133
Sliski, D. H., & Kipping, D. M. 2014, ApJ, 788, 148
Snellen, I. A. G., Koppenhoefer, J., van der Burg, R. F. J., et al. 2009, A&A, 497, 545
Sweigart, A. V., Greggio, L., & Renzini, A. 1989, ApJS, 69, 911
Sweigart, A. V., Greggio, L., & Renzini, A. 1990, ApJ, 364, 527
van Leeuwen, F. 2007, A&A, 474, 653
Veras, D., Mustill, A. J., Bonsor, A., & Wyatt, M. C. 2013, MNRAS, 431, 1686
Veras, D., Wyatt, M. C., Mustill, A. J., Bonsor, A., & Eldridge, J. J. 2011, MNRAS, 417, 2104
Verbunt, F., & Phinney, E. S. 1995, A&A, 296, 709
Villaver, E., & Livio, M. 2007, ApJ, 661, 1192
Villaver, E., & Livio, M. 2009, ApJL, 705, L81
Witte, M. G., & Savonije, G. J. 2002, A&A, 386, 222
Wright, J. T., Fakhouri, O., Marcy, G. W., et al. 2011, PASP, 123, 412
Wright, J. T., Upadhyay, S., Marcy, G. W., et al. 2009, ApJ, 693, 1084
Zahn, J. P. 1966, AnAp, 29, 489
Zahn, J.-P. 1977, A&A, 57, 383
Zahn, J.-P. 1989, A&A, 220, 112
Zieliński, P., Niedzielski, A., Wolszczan, A., Adamów, M., & Nowak, G. 2012, A&A, 547, A91